Published in final edited form as:

Cell Rep. 2022 May 17; 39(7): 110822. doi:10.1016/j.celrep.2022.110822.

Glutamate released by Cajal-Retzius cells impacts specific hippocampal circuits and behaviors

Max Anstötz[1,2,*], **Sun Kyong Lee**[1], **Gianmaria Maccaferri**[1,3,*]

[1]Department of Neuroscience, Feinberg School of Medicine, Northwestern University, Chicago, IL 60611, USA

[2]Institute of Anatomy II, Medical Faculty, Heinrich-Heine-University, Düsseldorf 40225, Germany

[3]Lead contact

SUMMARY

The impact of Cajal-Retzius cells on the regulation of hippocampal circuits and related behaviors is unresolved. Here, we directly address this issue by impairing the glutamatergic output of Cajal-Retzius cells with the conditional ablation of vGluT2, which is their main vesicular glutamate transporter. Although two distinct conditional knockout lines do not reveal major alterations in hippocampal-layer organization and dendritic length of principal neurons or GABAergic cells, we find parallel deficits in specific hippocampal-dependent behaviors and in their putative underlying microcircuits. First, conditional knockout animals show increased innate anxiety and decreased feedforward GABAergic inhibition on dentate gyrus granule cells. Second, we observe impaired spatial memory processing, which is associated with decreased spine density and reduced AMPA/NMDA ratio of postsynaptic responses at the perforant- and entorhino-hippocampal pathways. We conclude that glutamate synaptically released by Cajal-Retzius cells is critical for the regulation of hippocampal microcircuits and specific types of behaviors.

Graphical abstract

*Correspondence: max.anstoetz@northwestern.edu (M.A.), g-maccaferri@northwestern.edu (G.M.).

AUTHOR CONTRIBUTIONS

Conceptualization, M.A. and G.M.; electrophysiological experiments, M.A. and G.M.; western blot experiments, S.K.L.; imaging and reconstructions, M.A.; PCR experiments, M.A.; data analysis, M.A. and G.M.; writing – original draft, G.M.; writing – review & editing, G.M., M.A., and S.K.L. All authors have agreed on the interpretation of data and have approved the final version of the manuscript.

SUPPLEMENTAL INFORMATION

Supplemental information can be found online at https://doi.org/10.1016/j.celrep.2022.110822.

DECLARATION OF INTERESTS

The authors declare no competing interests.

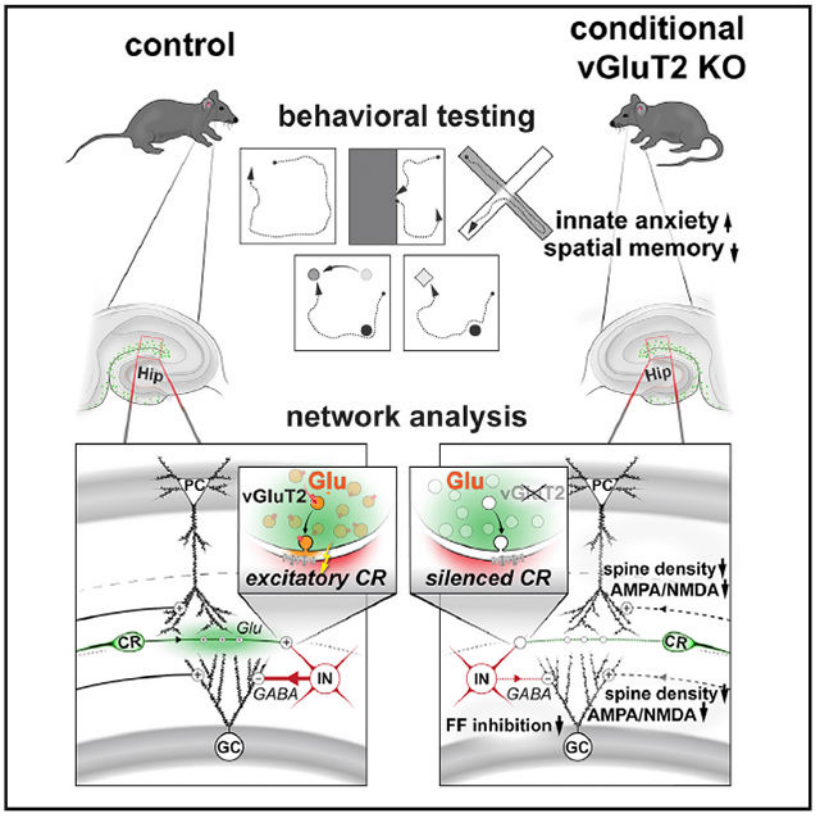

In brief

Anstötz et al. report that postnatal hippocampal Cajal-Retzius cells use vGluT2 as their main glutamate vesicular transporter. Conditional inactivation of vGluT2 in mice reveals both behavioral and network alterations. The observed results indicate the involvement of Cajal-Retzius cells in the regulation of innate anxiety/spatial memory and in potentially related neuronal circuits.

INTRODUCTION

Cajal-Retzius cells (CRs, Causeret et al., 2021) have long been considered transient neurons of the cortex that contribute to organizing its architecture during development (Gil et al., 2014). In particular, the synthesis and secretion of the glycoprotein reelin by CRs (D'Arcangelo et al., 1995; Ogawa et al., 1995) suggested a key link to the formation of cortical layers (Frotscher, 1998) because this latter process is impaired in reelin mutants (Caviness and Sidman, 1973a, 1973b; Goffinet, 1984; Rice and Curran, 2001). Consequently, most studies on CRs have focused on their complex intra- and extra-cellular non-synaptic signaling, which is required to perform their "project manager" role for the construction of the cerebral cortex (Villar-Cerviño and Marín, 2012). In contrast, the significance of CRs as synaptic sources of conventional neurotransmitters has remained elusive.

Despite early evidence pointing to a glutamatergic phenotype (del Río et al., 1995; Hevner et al., 2003; Ina et al., 2007), CR synaptic integration into the immature neocortex (Soda

et al., 2003) or hippocampus (von Haebler et al., 1993) was initially reported dubious. This, together with their rapid apoptotic disappearance in the postnatal neocortex (Derer and Derer, 1990; Chowdhury et al., 2010), reduced the perceived significance of their neurotransmitter output for fast network computations and/or developmental roles. However, more recent studies showing regional specificity of CR death (de Frutos et al., 2016; Ledonne et al., 2016) and their persistence in the mature hippocampus (Ledonne et al., 2016; Anstötz et al., 2016, 2018a) have renewed interest in their postnatal network functions. In fact, CRs are synaptically integrated into hippocampal circuits and establish input/output connections with specific subtypes of GABAergic interneurons (Quattrocolo and Maccaferri, 2013, 2014; Anstötz et al., 2016, 2018b).

Despite these advances, the impact of CR synaptic connectivity on hippocampal-related behaviors and network integration remains unclear.

Here, we have addressed these issues by generating two mouse lines with CR-specific deletion of their main vesicular glutamate transporter (vGluT2) and simultaneous expression of the opsin ChR2(H134R)-EYFP (Madisen et al., 2012). We show that the conditional ablation of vGluT2 augments innate anxiety and impairs spatial memory; we propose that these effects depend on the alteration of behaviorally relevant microcircuits, such as feedforward inhibition onto dentate gyrus granule cells (innate anxiety) and disrupted maturation of excitatory synaptic input from the entorhinal cortex (spatial memory).

RESULTS

In order to assess the effects of silencing the synaptic output of CRs, we used different Cre and floxed lines (see STAR Methods) to generate animals with the conditional deletion of vGluT2. For simplicity, we will refer to mice with/without the full conditional deletion of vGluT2 (but with the concurrent conditional expression of ChR2(H134R)-EYFP in both cases) as either ΔNp73-control/ΔNp73-knockout (KO) or PDE1c-control/PDE1c-KO (depending on the Cre line used: ΔNp73-Cre-IRES-GFP or PDE1c-Cre; see STAR Methods). Collectively, we will refer to ΔNp73-control and PDE1c-control mice as controls and to ΔNp73-KO and PDE1c-KO animals as KOs. Experimental values and statistical analyses are given in Table S1.

Conditional KO of vGluT2 in CRs does not trigger compensation from other vGluTs

First, we verified that the genetic manipulations introduced in KOs did not affect hippocampal CR densities. CRs were identified by their typical tadpole-like shape, location in the molecular layers (i.e., molecular layer of the dentate gyrus and stratum lacunosum moleculare of the hippocampus proper), and by their specific EYFP and p73 expression (Anstötz and Maccaferri, 2020; Figures 1A–1D). As shown in Figures 1C and 1D, the quantification of CRs (by p73 immunoreactivity) did not reveal significant differences in their linear densities along the hippocampal fissure, either between ΔNp73-control and ΔNp73-KO or between PDE1c-control and PDE1c-KO mice (Table S1). Second, although vGluT2 has been reported to be the main vesicular-glutamate transporter in embryonic neocortical CRs (Ina et al., 2007), we verified that this was also the case in the postnatal hippocampus. We used confocal imaging to study the expression of the vGluT1/vGluT2/

vGluT3 isoforms in synaptic terminals of CRs (specifically identified by membrane fluorescence due to EYFP expression). Immunohistochemical experiments revealed the predominant expression of vGluT2 compared with vGluT3 and the lack of vGluT1 in all control lines, thus confirming that vGluT2 remains CRs' main vesicular-glutamate transporter in the postnatal hippocampus (Figures 1E and 1F; Table S1). Third, we verified the absence of vGluT2 in CR terminals of KO animals and excluded compensation mediated by vGluT1 or vGluT3. As expected, vGluT2+ terminals were absent both in ΔNp73-KO and PDE1c-KO mice, with no changes in the density of vGluT1+ or vGluT3+ boutons (Figures 1E and 1F; Table S1). Taken together, these results predicted that conditional vGluT2 deletion in CRs would disrupt transmission onto their postsynaptic targets.

Conditional vGluT2 KO mice show the selective impairment of optogenetically evoked EPSCs in interneurons of the molecular layers

This prediction was tested by optogenetic experiments measuring CR-originated excitatory postsynaptic currents (EPSCs) in interneurons, which are a major cellular target of CRs (Anstötz et al., 2018b). Despite the similar size of photocurrents in CRs of control and KO mice (Figures 1G and 1H; Table S1), the amplitude of flash-evoked EPSCs in interneurons was reduced in KOs, consistent with what was expected from the silencing of CR synaptic output (Figures 1I and 1J; Table S1). Importantly, biocytin-filled interneurons from control and KO mice did not reveal differences in their dendritic lengths (Figures S1A and S1B; Table S1), thus ruling out the loss of postsynaptic domains as a cause of the decreased optogenetically evoked EPSC. Furthermore, the densities of GAD65/67 immunolabeled interneurons of the molecular layers (dentate gyrus molecular layer and hippocampus proper CA1 stratum lacunosum moleculare) remained similar in control versus KO mice (Figures S1C–S1F; Table S1).

Conditional KO animals retain a normal general hippocampal architecture

The observed lack of changes, however, does not exclude the potential presence of other hippocampal structural alterations. Therefore, we examined the architecture of the dentate gyrus and of the adjacent hippocampus proper subfield CA1 by measuring their areas and the relative thicknesses of their layers but found no differences in control versus KO lines (Figures S2A and S2B; Table S1). Furthermore, Sholl analysis of the dendritic lengths of granule (Figures S2C and S2D; Table S1) and CA1 pyramidal cells (Figures S2E and S2F; Table S1) failed to uncover alterations in KOs. These results are in apparent contrast to the hippocampal dysgenesis observed by Amelio et al. (2020) in mice with genetically reduced CR densities. However, under those conditions, loss of CRs was associated with reduced reelin levels. In contrast, we verified that reelin expression did not change in our KO lines. (Figure S3; Table S1). Therefore, the lack of cross-interference between the conditional genetic ablation of vGluT2 and reelin expression is the most likely explanation for these differences.

Enhanced innate anxiety and loss of CR-dependent feedforward inhibition in conditional KO mice

Next, we wondered whether conditional vGluT2 ablation in CRs could impact hippocampal-dependent behaviors. When the two genotypes were compared in open field tests (Figures

2A–2D, Table S1), KO mice showed a higher preference for the border versus the central area. As the normalized distance traveled (see STAR Methods) was not different between the two genotypes, major motor impediments were ruled out. Center avoidance was also reflected by the higher speeds of KO mice in the central region. To strengthen the interpretation that increased thigmotaxis reflected augmented innate anxiety (Simon et al., 1994), we performed more specific tests, such as the elevated plus maze (Figures 2E–2H; Table S1; Rodgers and Dalvi, 1997) and light/dark transition tasks (Figures 2I–2L; Bourin and Hascoët, 2003). These tests evaluate the preference of mice for more protected areas (closed arm of the elevated plus maze and dark area in the light/dark transition test) relative to open/bright spaces. Compared with control animals, KO mice spent more time in the closed arm of the elevated plus maze, with fewer center entries and a decreased normalized distance traveled (Table S1). When the same individual animals were challenged in the light/dark transition test, KO mice showed a significant preference for the dark compartment, with fewer entries to the illuminated part of the arena, despite a similar normalized distance traveled (Table S1). The lack of differences in the normalized distance traveled in the light/dark transition test (similar to what was found in the open field) indicates that the lower values measured in the elevated plus maze test reflect decreased exploratory activity, as opposed to motor impairment.

Taken together, these results point to increased innate anxiety in KO mice. Consequently, we wondered whether we could detect alterations in hippocampal circuits known to be associated to the regulation of this emotional state. In particular, as deficits of the activity of $GABA_A$ receptors in the dentate gyrus have been causally linked to increased anxiety (Engin et al., 2016), we compared the magnitude of CR-driven feedforward GABAergic inhibition on granule cells of control versus KO mice (Figure 3A). Optogenetic stimulation of CRs evoked disynaptic feedforward GABAergic currents in control animals, which were absent in KO mice (Figures 3B and 3C; Table S1). The disynaptic nature of the feedforward inhibitory postsynaptic currents (IPSCs) was verified by testing its sensitivity to AMPA- and $GABA_A$-type receptor antagonists. As expected, feedforward IPSCs were blocked by the application of either NBQX or gabazine (Figures 3D and 3E; Table S1). In addition, in agreement with its compound and polysynaptic nature, flash-evoked events showed longer latencies and slower kinetics compared with monosynaptic excitatory responses recorded from interneurons (Figures 3F and 3G). Thus, our results from behavioral and slice experiments are consistent with the decrease in CR-dependent feedforward inhibition being a potential mechanism mediating the emotional dysregulation of KO mice.

Selective impairment of spatial memory and morpho-functional alterations of the perforant- and direct entorhino-hippocampal pathways of conditional KO mice

Next, we investigated two different forms of hippocampal-dependent cognitive functions, i.e., spatial and recognition memory (Broadbent et al., 2004). Spatial memory was assessed by measuring the time spent close to a specific object before and after it was moved to a different location, relative to the overall time spent in the proximity of both objects (object-location test). In contrast to controls, KO animals did not show a physiological increase in the relative time spent in the proximity of the object moved to the new location during the testing phase (Figure 4A and 4B; Table S1). However, both genotypes performed

similarly when recognition memory was assessed by the novel-object-recognition task, with a familiar object being replaced by an unfamiliar one during the testing phase. Both control and KO mice increased their preference for the novel object (Figures 4C and 4D; Table S1).

The impairment in spatial memory suggests disruptions in hippocampal sensory processing. Physiologically, sensory information from the entorhinal cortex is conveyed to the hippocampus by synapses established (in the molecular layers) on the dendritic spines of granule (perforant pathway; Blackstad, 1975) and pyramidal cells (direct entorhino-hippocampal pathway; Desmond et al., 1994). Therefore, we evaluated structural changes in these pathways by estimating spine densities at layer-specific postsynaptic domains in the dentate gyrus and CA1 hippocampal subfield (Figures 4E and 4F; Table S1).

In particular, for granule cells, we calculated spine densities on the distal half of their dendrites (which includes the outer and part of the middle molecular layer of the dentate gyrus), whereas for CA1 pyramidal neurons, we examined dendritic segments located in stratum lacunosum moleculare. Compared with control animals, spine density in KO mice was decreased by ~30% in granule cells and by ~40% in pyramidal neurons, suggesting loss of synaptic excitatory input. However, the observed decrease was selective for strata innervated by CRs, as it was absent when the same analysis was repeated on the basal dendrites of pyramidal cells in stratum oriens (Figures 4E and 4F; Table S1). In addition, electrical stimulation of the molecular layers produced EPSCs with lower AMPA/NMDA ratios in KO versus control lines (estimated as AMPA/NMDA* ratios; see STAR Methods). In contrast, no differences between the two genotypes were observed when the stimulation was restricted to stratum oriens to activate excitatory inputs to the basal dendrites of CA1 pyramidal cells (Figures 4G and 4H; Table S1). Importantly, the decrease in spine density cannot be explained by loss of putative synapses established by CRs themselves on principal neurons for several reasons. First, when CRs establish synapses, they are made on dendritic shafts and not on spines (~85% [Anstütz et al., 2016] and 100% [Marchionni et al., 2010]). Second, CR boutons often lack postsynaptic specializations (Marchionni et al., 2010), suggesting that the rare responses observed in principal cells are mediated by volume transmission (Marchionni et al., 2010; Quattrocolo and Maccaferri, 2014). Third and last, optogenetic stimulation of CRs (under the same experimental conditions used to evoke EPSCs in interneurons as in Figure 1) triggered either no EPSCs in granule cells or detectable responses only in a minor proportion of CA1 pyramidal cells (Figure S4; Table S1), similar to what was previously reported (Quattrocolo and Maccaferri, 2014). Taken together, these parallel structural and functional alterations in layer-specific excitatory synaptic input of KO mice is consistent with our hypothesis of impaired entorhinal-hippocampal sensory processing, which then leads to disruption of spatial memory.

DISCUSSION

Our work reveals the involvement of CR glutamatergic output in shaping specific hippocampal microcircuits and hippocampal-dependent behaviors. In particular, our data underscore the significance of CR synaptic transmission, independently of reelin. Although previous work has already suggested the requirement of CRs for hippocampal-dependent

behaviors, different manipulations (also affecting reelin) were used. For example, genetic depletion of CRs (with a parallel reduction in reelin levels at embryonic stages critical for hippocampal development) was shown to be associated with impaired learning and memory in adulthood (Amelio et al., 2020). Furthermore, the systemic pharmacological inhibition of the progesterone receptor (which is transiently expressed by CRs; Newell et al., 2018) was reported to cause reelin accumulation in CRs and impaired episodic-like memory in mice (Newell et al., 2021). However, neither of these studies measured the synaptic output of CRs and the less-selective manipulations used produced more complex outcomes. In contrast, our work points directly to the involvement of CR glutamatergic output in the regulation of anxiety and selective forms of memory.

Mechanistically, we propose that the critical changes underlying our observations *in vivo* are the loss of CR-driven feedforward GABAergic input to granule cells (innate anxiety; Engin et al., 2016) and the morpho-functional impairment of critical synapses receiving sensory information from the entorhinal cortex (spatial memory; Moser et al., 2017). The lack of feedforward inhibition is easily accounted for by a decreased excitatory drive from CRs to GABAergic interneurons. Regarding the excitatory drive to CRs themselves, which is also required to produce feedforward inhibition, it is important to note that even if postnatal hippocampal CRs do not receive significant direct glutamatergic input (Marchionni et al., 2010), they can be activated by excitatory GABAergic input from neurogliaform cells and oriens-lacunosum moleculare (O-LM) interneurons (Quattrocolo and Maccaferri, 2013).

The most parsimonious explanation for the reduction of spine density and AMPA/NMDA ratios observed in KO mice is the loss of direct neuro-modulatory glutamatergic trophic action on developing excitatory synapses (Kwon and Sabatini, 2011; Mattison et al., 2014). However, glutamatergic output of CRs may also indirectly trigger the release of additional glutamate (Rose et al., 2018) and/or other unidentified factors from glial cells. The parallel decrease in spine densities and AMPA/NMDA ratios suggests a maturation delay of the postsynaptic side of excitatory connections from the entorhinal cortex (Durand et al., 1996; Hanse et al., 2013). Alternatively, the decreased spine density in KO mice could reflect impaired development of presynaptic innervation similar to what described by Del Río et al. (1997) in entorhino-hippocampal co-cultures *in vitro*. Lastly, our data are consistent with findings in the neocortex indicating that CR density (which we propose relates to its glutamatergic output) is a critical determinant of functional wiring and spine formation during development (de Frutos et al., 2016; Riva et al., 2019).

With regard to our behavioral results, it is interesting to note that the ontogeny of object and associative spatial memory follows different time courses in developing rodents (Ainge and Langston, 2012). In fact, the neural systems supporting object-recognition memory appear to possess established adult-like qualities earlier than the circuits related to allocentric spatial memory, which take longer to mature and do not reach adult levels of specificity and stability until the fourth or fifth postnatal week (Langston et al., 2010; Wills et al., 2010; Ainge and Langston, 2012). These observations may explain why the developmental immaturity of the perforant- and/or entorhino-hippocampal pathway (indicated by reduced spine densities and lower AMPA/NMDA ratios; Durand et al., 1996; Hanse et al., 2013) impairs spatial memory but not object recognition. Therefore, we propose that glutamatergic

output from CRs regulates the maturity of nearby synaptic sites established by afferent inputs to the hippocampal molecular layers and functions as a "synaptic developmental clock.' Assuming that this mechanism is blocked in KO mice, our hypothesis would predict an "immature" phenotype of place cells recorded from these animals, with properties similar to those described in young rodents at the beginning of their navigational experience (Langston et al., 2010; Wills et al., 2010). Future work will be necessary to confirm/disprove this hypothesis. Lastly, the involvement of CRs in all of the aforementioned processes suggests their potential relevance for aging and neurological disorders, as their density in the human hippocampus is affected by both conditions (Blümcke et al., 1999; Baloyannis, 2005). Therefore, it will be interesting to study whether loss of synaptic output from these cells may contribute to some aspects of the associated emotional/cognitive impairments.

Limitations of the study

First, specificity of Cre expression for a particular cellular population may be difficult to achieve (Hu et al., 2013) and may lead to misinterpretations (Müller-Komorowska et al., 2020). We have addressed this point by using two distinct Cre lines. The convergence of results argues in favor of the CR specificity of the reported effects. Second, although the genetic ablation of glutamatergic output from CRs is an unequivocal mechanistic starting point, we recognize that the behavioral effects observed in KO animals likely depend on complex chains of events and molecular/cellular networks. Although we consider our interpretations to be the simplest explanations based on current knowledge, additional (or even alternative) mechanisms cannot be ruled out. For example, because of the technical difficulty of detecting synaptic events generated at distal dendritic sites (relative to the proximal position of somatic electrodes), feedforward inhibition was only measured in granule cells and not in CA3 pyramidal neurons, whose $GABA_A$ receptors are also involved in anxiety regulation (Engin et al., 2016). Therefore, we cannot exclude that this additional circuit may play a role in creating the behavioral phenotype of KO mice. Lastly, we measured spine density at postsynaptic domains of granule cells receiving synaptic inputs from both the lateral and medial perforant paths, which are traditionally believed to mediate different spatial/non-spatial computations (Hargreaves et al., 2005). However, this absolute dichotomy is constantly undergoing re-evaluation and it cannot be excluded that, albeit to different degrees, both inputs are involved and cooperate in supporting hippocampal spatial selectivity (Hales et al., 2014; Wang et al., 2018).

STAR★METHODS

RESOURCE AVAILABILITY

Lead contact—Further information and requests for resources and reagents should be directed to and will be fulfilled by the lead contact, Gianmaria Maccaferri (g-maccaferri@northwestern.edu).

Materials availability—All mouse lines generated in this study can be obtained by the appropriate breeding of lines available commercially (Jackson Labs, MMRRC) except form the ΔNp73-Cre-IRES-GFP mouse strain that requires permission from the donating investigator (Dr Fadel Tissir, UC Louvain, Belgium, fadel.tissir@uclouvain.be).

Data and code availability

- All data reported in this paper will be shared by the lead contact upon request.
- This paper does not report original code.
- Any additional information required to reanalyze the data reported in this paper is available from the lead contact upon request.

EXPERIMENTAL MODEL AND SUBJECT DETAILS

Mice—All experiments were performed with the approval of Northwestern University Institutional Animal Care and Use Committee, and in accordance with the Guide for the Care and Use of Laboratory Animals [National Institutes of Health (NIH)]. Both female and male mice were used. All animals were subject to regular veterinary inspection and maintained on a conventional 14hr light/10hr dark cycle with free access to food and water.

Transgenic mice used for the experiments were produced by appropriately breeding mouse lines expressing Cre (under the control of promoters active in CRs) with floxed and STOP-floxed strains. In particular, we used the two following Cre lines: ΔNp73-Cre-IRES-GFP (Tissir et al., 2009) and PDE1c-Cre (strain: B6.FVB(Cg)-Tg(Pde1c-cre)IT146Gsat/Mmucd, Anstötz et al., 2018a). The ΔNp73-Cre-IRES-GFP line was estimated by Riva et al. (2019) to target approximately 80% of CRs [namely hem-derived CRs of Wnt3a lineage and septum and eminentia thalami-derived CRs of Dbx1 lineage (Yoshida et al., 2006; Tissir et al., 2009; Griveau et al., 2010)]. PDE1c is expressed by CRs (Osheroff and Hatten, 2009), and the estimated postnatal density of hippocampal CRs in PDE1c-Cre (tdTomato) reporter mice is similar to values measured using Wnt3a-IRES-Cre (Anstötz et al., 2018a), which suggests that the PDE1c-Cre line also targets hem-derived CRs of Wnt3a lineage (Louvi et al., 2007). For this reason, we have consistently replicated our results using both the ΔNp73-Cre-IRES-GFP and PDE1c-Cre line.

vGluT2 floxed mice (strain, STOCK Slc17a6tm1Lowl/J) were used to obtain conditional ablation of vGluT2, whereas the STOP-floxed-ChR2(H134R)-eYFP strain (B6;129S-Gt(ROSA)26Sortm32(CAG-COP4*H134R/eYFP)Hze/J, see Quattrocolo and Maccaferri, 2014), was used to drive conditional expression of ChR2(H134R)-eYFP.

Control animals obtained from the ΔNp73-Cre-IRES-GFP line [at the same time $Cre^{+/-}$, conditional $vGluT2^{+/-}$, and conditional ChR2(H134R)-$eYFP^{+/-}$] were compared to knockouts for vGluT2 [at the same time $Cre^{+/-}$, conditional $vGluT2^{-/-}$, and conditional ChR2(H134R)-$eYFP^{+/-}$]. Similarly, control mice from the PDE1c-Cre line [at the same time $Cre^{+/-}$, conditional $vGluT^{+/-}$, and conditional ChR2(H134R)-$eYFP^{+/-}$] were compared to knockouts for vGlut2 [at the same time $Cre^{+/-}$, conditional $vGluT2^{-/-}$, and conditional ChR2(H134R)-$eYFP^{+/-}$]. Only for the data of Figures 1H–1J, the control group for the PDE1c-Cre line included pooled results from $vGluT2^{+/+}$ and conditional $vGluT2^{+/-}$ mice [in both cases $Cre^{+/-}$ and conditional ChR2(H134R)-$eYFP^{+/-}$] because no differences were found in the amplitude of optogenetically evoked EPSCs recorded from interneurons in these two groups. This confirms the report that a single vesicular glutamate transporter may be sufficient to fill a synaptic vesicle (Daniels et al., 2006). Animals were genotyped

by Northwestern Center for Comparative Medicine using the commercial services of Transnetyx (Cordova, TN).

METHOD DETAILS

Electrophysiology

Slice preparation: Hippocampal slices (350 μm thick) were cut from P21-P31 mice. After deep anesthesia with isoflurane, animals were decapitated, and their brain quickly extracted and stored into a small container filled with chilled modified artificial cerebral spinal fluid (ACSF) of the following composition (in mM): 130 NaCl, 24 $NaHCO_3$, 3.5 KCl, 1.25 NaH_2PO_4, 1 $CaCl_2$, 2 $MgCl_2$, 10 glucose, saturated with 95% O_2, 5% CO_2 at pH 7.4. Transverse sections were prepared using a vibrating microtome (VT1200 S, Leica Biosystems Inc., Buffalo Grove, IL), incubated at 34–35°C for at least 30 min, and then stored at room temperature until use.

Whole-cell recordings: Neurons were visualized using a direct microscope (Scientifica, Clarksburg, NJ) with oblique illumination and a 60X infrared water-immersion objective (Olympus America, Waltham, MA) connected to an infrared camera system (Zyla, Andor USA, Concord, MA). Slices were superfused with preheated ACSF of the following composition (in mM): 130 NaCl, 24 $NaHCO_3$, 3.5 KCl, 1.25 NaH_2PO_4, 2 $CaCl_2$, 1 $MgCl_2$, 10 glucose, saturated with 95% O_2, 5% CO_2 at pH 7.4 and maintained at a constant temperature (31–33°C) by a temperature controller (TC-324B, Warner Instruments, Holliston, MA). Cajal-Retzius cells were recognized by their location, typical tadpole-like shape, and eYFP fluorescence. Interneurons of the hippocampal molecular layers (molecular layer of the dentate gyrus and stratum lacunosum-moleculare of the CA1 subfield of the hippocampus proper) were selected according to their localization, preferably close to the fissure (Quattrocolo and Maccaferri, 2014). Whole-cell patch-clamp pipettes were pulled from borosilicate glass capillaries (Prism FLG15, Dagan Corporation, Minneapolis, MN) and had a resistance of 3–5 MΩ when filled with the following intracellular solution (in mM): 125 Cs-methanesulfonate, 0.3 GTP-Na, 4 ATP-Mg_2, 16 $KHCO_3$, 10 QX-314Cl and 0.3–0.5% biocytin (equilibrated with 95% O_2, 5% CO_2 to pH 7.3). Recordings were performed using a Multiclamp 700A amplifier (Molecular Devices, San Jose, CA). Signals were filtered at 6 kHz and digitized at 20 kHz using a Digidata 1550A and the Clampex 10 program suite (Molecular Devices). Voltage-clamp recordings were performed at the holding potential indicated in the text and/or legends.

Optogenetic and electrical stimulation: Light stimulation was achieved by a collimated LED (Prizmatix Ltd., Holon, Israel) attached to the epifluorescence port of the microscope. Brief light flashes (1–5 ms) were directed to the molecular layers of the slice in proximity of the recorded neuron via a mirror coupled to a 60X objective. Stimulation was repeated for at least three times. Electrical field stimulation was generated by Pt/Ir monopolar (FHC, Bowdoin, ME) electrodes attached to a stimulus isolator (Iso-Flex, AMPI, Jerusalem, Israel) delivering current pulses (1 mA for SLM, 0.65 mA for SO, and 0.4 mA for ml) of 60 μs duration. Stimulation was repeated 20 times. All the optogenetically- and electrically evoked EPSCs/IPSCs shown in the illustrations are averages of responses from all the cells recorded in the experiments.

Immunohistochemistry—Mice (P30) were anesthetized by intraperitoneal injection of Euthasol (calculated to yield a dose of pentobarbital of 300 mg/kg of bodyweight) and perfused with 0.9% NaCl saline followed by 4% paraformaldehyde (PFA) in 0.1 M phosphate buffer (PB), pH 7.4. After perfusion, brains were extracted from the skull and transferred to fixative solution at 4°C for at least 24 h. The hippocampus was cut transversally in serial slices of 50 μm thickness on a Leica VT 1000 vibratome and collected free-floating in 0.01 M PBS.

Sections were preincubated free-floating in a blocking solution containing 5% normal goat serum (NGS), 1% bovine serum albumin (BSA) and 0.5% Triton X-100 in PBS for 1 h at room temperature (RT), followed by the addition of the appropriate primary antibodies (rabbit anti-p73, mouse anti-reelin, rabbit anti-GAD67, rabbit anti-vGluT1, rabbit anti-vGluT2, rabbit anti-vGluT3, rabbit anti-GAD65/ 67, all 1:500, see Key resources table) at 4°C overnight. Slices were then washed 3 × 15 min with fresh PBS and incubated free-floating in a solution of 5% NGS, 1% BSA in PBS, containing the secondary antibodies (Alexa Fluor 568 goat anti-rabbit IgG, Alexa Fluor 568 goat anti-mouse IgG, Alexa Fluor 647 goat anti-rabbit, Alexa Fluor 647 goat anti-mouse IgG all 1:500, see Key resources table) at RT for 1 h. Finally, sections were washed 3 × 15 min with PBS, with the second washing step containing DAPI (1:100,000, see Key resources table) to achieve fluorescent nuclear counterstaining. Slices were then mounted and coverslipped using Mowiol mounting medium.

Biochemistry

Western Blots: Hippocampi from P30 mice were dissected out on iced saline and homogenized in ice cold RIPA lysis buffer (see Key resources table). Homogenates were sonicated on ice for 30 s and centrifuged at 15,000 × g, 4°C for 30 min. Supernatants were collected, and their protein concentration was measured by bicinchoninic acid (BCA) colorimetric assay (see Key resources table). Sample (25 μg of protein) were taken and diluted with 1X RIPA lysis buffer, 4X LDS sample buffer (see Key resources table), and 10X NuPAGE reducing agent (see Key resources table). Diluted samples were warmed at 70°C for 10 min and then electrophoresed on 3–8% NuPAGE Tris-Acetate gel (see Key resources table) at 150 V. Separated protein bands were transferred to low fluorescence polyvinylidene fluoride membranes (PVDF) (see Key resources table) at 30 V for 1 h in NuPAGE transfer buffer (see Key resources table) containing 0.1% NuPAGE antioxidant (see Key resources table). The presence of proteins was confirmed in Ponceau S staining solution (see Key resources table), and membranes were washed in Western Dot Blocking Buffers (part of the appropriate WesternDot™ kit, see Key resources table) at RT for 1 h. Membranes were then incubated with primary antibodies (mouse anti-reelin 1:1000, and mouse anti-α-Tubulin 1:50000, see Key resources table) at 4°C, overnight. The following day, membranes were washed with 1× Western Dot Wash Buffer [50 mM Tris-HCl, 150 mM NaCl, 0.05% Tween 20, pH 7.4] (included in the appropriate WesternDot™ kit, see Key resources table) 3 × 10 min and then incubated with secondary antibodies included in the WesternDot™ kits (Biotin XX-goat anti-mouse IgG, or Biotin XX-goat anti-rabbit IgG, 1:500, see Key resources table) diluted in 1× Wash Buffer at RT for 1hr. Excessive secondary antibodies were washed out in 1X Western Dot Wash Buffer 3 × 10 min, and the membrane was incubated with

QDot625® streptavidin conjugate (included in the appropriate WesternDot™ kit, see Key resources table) diluted in 1X Wash Buffer at RT for 1 h in darkness. After completion of the BiotinXX-streptavidin reaction, membranes were washed in 1X Wash Buffer 3 × 10 min and then UV illuminated by ChemiDoc XRS imaging system (BioRad, Hercules, CA) to visualize QDot625® fluorescence.

Anatomy

Cell reconstructions: Biocytin-filled neurons were fixed in 4% PFA in 0.1 M PB at 4°C for at least 24 h. Endogenous peroxidase activity was quenched with a 3% H_2O_2 solution for 15 min. Sections were incubated overnight at 4°C in avidin-biotinylated-HRP complex (Vectastain ABC Elite kit, see Key resources table) with 0.1% Triton X-100 in PB, followed by a peroxidase reaction with 3,3'-diaminobenzidine tetrahydrochloride as a chromogen. Cells were revealed by adding 0.025% H_2O_2, and the reaction was stopped when dendritic and axonal processes were clearly visible under light microscopy examination. After several washing steps in 0.1 M PB, slices were postfixed with 0.1% OsO_4 in PB (1–2 min), and then mounted on slides with Mowiol® 4-88 (see Key resources table). Sections with biocytin-filled granule cells and pyramidal cells were incubated in 0.5% Triton X-100 in PBS for 1 h at RT, followed by 1:1000 streptavidin-Alexa 568 (see Key resources table) in 0.5% Triton X-100 in PBS at RT. Sections were washed 3 × 15 min in PBS, mounted with Mowiol and coverslipped. Cells were reconstructed using a Zeiss Axioskop 2 equipped with Neurolucida 11 software suite (MBF bioscience, Williston, VT).

Golgi stain: This procedure was performed with a FD Rapid Golgi Stain Kit (see Key resources table) according to the detailed manufacturer's protocol. Briefly, mice (P30) were deeply anesthetized with isoflurane and then decapitated. Brains were extracted from the skull, rinsed with distilled water, and transferred to impregnation solution A/B for 14 days and then to solution C for 3 days. Horizontal brain slices (200 μm thickness) were cut using a Leica VT 1000 vibratome and mounted on glass slides. Slices were rinsed 2 × 4 min in distilled water and transferred into staining solution D/E for 10 min under visual inspection. After rinsing 2 × 4 min in distilled water, sections were dehydrated in ethanol with incremental concentrations (50%, 75%, 95%) for 4 min each and finally in 4 × 4 min in 100% ethanol. Slices were then cleared 3 × 4 min in xylene and coverslipped with Permount mounting medium.

Behavior

General methods for all behavioral experiments: Each mouse was handled for one minute in the five days preceding the experiments. Before testing, they were acclimated to the room for at least 3 h by remaining in their cage with food and water ad libitum.

Open field, object location and novel object recognition tests: In most cases, the same animals were studied according to the following sequence: day1: open field test, day2: open field test, day3: object location test, day4: no experiment, day5: novel object recognition test. On day1, the age (postnatal day) of the mice used was: 30 ± 1 (ΔNp73-control), 30 ± 1 (ΔNp73-KO), 32 ± 2 (PDE1c-control), and 31 ± 1 (PDE1c-KO).

The arena used for these tests was made of a white open acrylic cube (40 cm × 40 cm × 40 cm) with spatial cues placed on its walls. Behavior was recorded with a camera held by a post and movement was tracked using the Stoelting ANY-maze software suite (Stoelting Co., Wood Dale, IL). The arena and objects were thoroughly cleaned and wiped with 70% ethanol between experiments.

For open field experiments, mice were released into the arena and tracked for 10 min during two consecutive days.

For object location tests, the arena contained two wooden objects (object1 and object2, both 20 mm radius ball) and mice positions were recorded for 10 min (training session). Interaction with an object was defined by the head of the mouse being within a 30 mm radius from the center of the object. After the training session, the mouse was returned to the cage for 20 min, and then re-introduced into the arena for the testing phase (10 min), with one of the objects (object2) moved to a new location.

For novel object recognition test, mice were exposed (during the training phase) to the same objects used for the object location test (for 10 min, object1 and object2). After a 20 min interval, animals were returned to the arena for the testing session (10 min), with object1 unchanged and object2 replaced (in the same location) by object3 (of different shape and color: cube of 40 mm × 40 mm × 40 mm).

Light/dark transition task and elevated plus maze test: The same animals were studied for three consecutive days, each day according to the following sequence: light/dark transition task followed by the elevated plus maze test (2 h interval). Arenas were thoroughly cleaned and wiped with 70% ethanol between experiments. On day1, the age (postnatal day) of the mice used was: 29 ± 1 (ΔNp73-control), 29 ± 1 (ΔNp73-KO), 29 ± 1 (PDE1c-control), and 28 ± 1 (PDE1c-KO).

For the light/dark transition task, mice were placed in an arena (same dimensions of the one used for the open field test) divided in two sections of equal size, communicating via a central opening (semi-circular, with a radius of about 3 cm). The first compartment was open, whereas the second was fully enclosed (apart from the central opening) by black acrylic material and not exposed to the light. Following release in the open section, mice were allowed to freely enter/exit each compartment for 10 min and their positions were tracked in the uncovered area.

For the elevated plus maze test, mice were placed in a plus sign shaped arena with two open and two closed arms (with black opaque walls on both sides, 40 cm in height), and an open central area. The dimensions of the open and closed arms were identical (40 cm × 8 cm), and the central open area was 8 cm × 8 cm. The entire structure was mounted on four posts at an elevation of 50 cm above ground. Animals were released in the center area and their positions tracked for 10 min.

Molecular biology

Real time quantitative polymerase chain reaction: Hippocampal tissue was homogenized by up-down pipetting with decreasing needle size (20 G–27 G needles, B Braun, Melsungen, Germany) in RLT buffer containing RNAse inhibitor (see Key resources table). Final tissue homogenization was achieved using QIAshredder columns (see Key resources table) for PCR analysis, according to the manufacturer's instructions. The RNeasy Mini Kit (see Key resources table) was used for mRNA isolation, including digestion with DNase I (see Key resources table). Elution of mRNA was done in RNase free water. RT2 First Strand Kit (see Key resources table) was used to synthesize cDNA, following the manual. Mouse-specific TaqMan probe for reelin (see Key resources table) and Hypoxanthin-Guanin-Phosphoribosyltransferase (see Key resources table) and a StepOnePlusTM Real-Time PCR System with 96-well plates (Thermo Fisher Scientific, Waltham, MA), were used.

QUANTIFICATION AND STATISTICAL ANALYSIS

Synaptic currents—Peak amplitude of optogenetically evoked excitatory and inhibitory postsynaptic currents was measured using Clampfit 10 functions (Molecular Devices). AMPA/NMDA ratios of electrically evoked responses were calculated by dividing the absolute peak of the inward current at a holding potential of −60 mV by the amplitude of the outward current at +40 mV, measured 75 ms after its peak (AMPA/NMDA* ratio). Because of the different decay kinetics of AMPA- vs NMDA mediated currents, this method allows to measure a pure NMDA receptor-mediated component when the AMPA receptor-mediated current has already fully decayed to baseline (Hestrin et al., 1990). All experiments were performed in the constant presence of gabazine (12.5 μM). Averaged traces were used for quantification except for the optogenetically evoked EPSCs on interneurons, which were measured on the first response.

Cajal-Retzius cell linear density—Cajal-Retzius cells were identified and quantified by their p73 immunoreactivity (Anstötz and Maccaferri, 2020) using a Zeiss Axioscope2 (Carl Zeiss Microscopy, LLC, White Plains, NY) equipped with Neurolucida 11 software suite (MBF bioscience). Hippocampal molecular layers (molecular layer of the dentate gyrus and stratum lacunosum-moleculare of the CA1 subfield of the hippocampus proper) were chosen as regions of interest and linear cellular densities were calculated as previously described in detail (Anstötz et al., 2016, 2018a).

GABAergic interneuron density—GABAergic interneurons were identified by their GAD65/67 immunoreactivity using a Zeiss AxioImager M1 (Carl Zeiss Microscopy, LLC, White Plains, NY) equipped with Neurolucida 11 software suite (MBF bioscience) under a 40X/NA 1.3 lens. The molecular layers of the hippocampus (molecular layer of the dentate gyrus and stratum lacunosum-moleculare of the hippocampus proper CA1 subfield) were chosen as regions of interest. Quantification was performed on 50 μm thick sections and interneurons were counted as number of DAPI-stained GAD65/67 immunoreactive cells. Densities were finally obtained by dividing the number of cells per area of the region of interest.

Volumetric density of terminals with specific vGluT immunoreactivity— Confocal microscopy stacks covering an area of 125 μm × 125 μm (resolution of 125 nm/pixel and z-step size of 500 nm) were acquired using a Nikon A1 microscope (Nikon Instruments Inc. Melville, NY) equipped with a 100X/NA 1.4 lens and imported into the Neurolucida 11 software suite (MBF bioscience). Axonal varicosities in the eYFP channel that contained an immunofluorescence signal for either the vGluT1, vGluT2 or vGluT3 transporters were identified as terminals and marked according to their immunoreactivity. Volumetric densities were calculated by dividing the number of terminals by the volume of the stack.

Western blot optical density—QDot625® fluorescence in membranes was analyzed by Quantity One software (BioRad). The values obtained for the various reelin isoforms were normalized for α-tubulin.

Reelin immunoreactivity in Cajal-Retzius cells relative to GABAergic interneurons—eYFP fluorescence, as well as GAD67 and reelin immunolabeling were detected with a Nikon A1 confocal microscope equipped with a 63X/NA1.4 lens. Stacks covering an area of 150 μm × 150 μm with a resolution of 300 nm/pixel were acquired and z-step size of 1 μm. The acquired stacks were then imported into ImageJ (Schneider et al., 2012) and individual eYFP+ or GAD67+ cells outlined as regions of interest. The integrated pixel intensity in the region of interest was measured and divided by its area. Local background intensity was subtracted from the value. The ratio of reelin immunoreactivity in CR cells over GABAergic interneurons was calculated from the averages obtained in the two cell groups.

Sholl analysis—Post hoc morphometric data were analyzed with Neurolucida Explorer software (Anstötz and Maccaferri, 2020). Sholl analysis was performed by measuring dendritic lengths within a 50 μm initial radius and in the circular crowns obtained by 50 μm increments for granule cells, interneurons, and basal dendrites of pyramidal cells. In case of the apical dendrites of CA1 pyramidal cell both the starting radius and increment were 100 μm.

Spine density—Randomly selected dendritic segments (~60 μm length) in the distal half of the molecular layer of the dentate gyrus or within either stratum lacunosum moleculare or stratum oriens of the CA1 region were analyzed. Spines were observed and identified with a Zeiss Axioskop 2 equipped and with a Neurolucida System and a 100X/NA1.4 lens. Spine density was obtained by dividing their number of by the dendritic length.

Open field test—The time spent by the mice at specific locations in the arena were measured with the ANY-maze software suite. The results of the experiments obtained in day1 and day2 were averaged and heat maps built with Origin 2020 software (Originlab Corporation, Northampton, MA). Relative time in the center area was calculated by dividing the time spent by the animals in the center area (36 cm × 36 cm) by the entire duration of the test. Center/border speed was calculated as the ratio of the average velocity of the mice in the center area (36 cm × 36 cm) over the border (remaining area of the 40 cm × 40 cm arena). Normalized distance was calculated as the total distance traveled in the entire arena,

divided by the duration of the test. This was required to have consistent measurements with the light/dark transition test (see below), where only movement in the open compartment may be tracked.

Light/dark transition task—Relative time in light was calculated by dividing the time spent by the animals in the open compartment by the entire duration of the test. Number of light entries was calculated as the number of transitions from the covered compartment into the open section of the arena. Lastly, as movement could not be tracked in the dark area, the normalized distance in light was calculated by dividing the total distance traveled in the open compartment by the time spent in this section.

Elevated plus maze test—Relative time in the open arm was calculated by dividing the time spent by the animals in the open arm by the entire duration of the test. Number of center entries were calculated as the number of times mice would enter the central area. Normalized distance was calculated by dividing the total traveled distance by the duration of the test.

Object location test—The “relative time with object” shown for this experiment was calculated as time_object2/(time_object1+time_object2) × 100, where object2 was the object moved to a new location.

Novel object recognition test—The “relative time with object” for this experiment was calculated as time_object2/(time_object1+time_object2) × 100 for the training phase and time_object3/(time_object1+time_object3) × 100 for the testing phase. Object2 was the original object in the training phase replaced by the new object3 in the testing phase.

Real time quantitative polymerase chain reaction—mRNA levels were calculated using the $2(-\Delta\Delta C(T))$ described in detail in reference (Livak and Schmittgen, 2001).

Statistical methods—Statistics were performed using the Mann-Whitney U test comparing two groups or by a ranked repeated measures (Two-Way) ANOVA comparing multiple cell measurements groups/categories in Origin 2020 (OriginLab Corporation). Level of significance for individual tests was chosen as $p < 0.05$. The level of significance in the figures is indicated as follows: ns: $p > 0.05$; *: $p < 0.05$, **: $p < 0.01$; ***: $p < 0.001$. Box plots in the illustrations indicate the median (middle dash), the lower and upper quartile (box borders), and minimum and maximum values (whiskers).

Supplementary Material

Refer to Web version on PubMed Central for supplementary material.

ACKNOWLEDGMENTS

We thank Drs. Jelena Radulovic and Marco Martina for comments and Dr. Fadel Tissir for allowing us to use the ΔNp73-Cre-IRES-GFP mouse line. This work was supported by a grant from the National Institute of Neurological Disorders and Stroke (NS064135) to G.M.

REFERENCES

Ainge JA, and Langston RF (2012). Ontogeny of neural circuits underlying spatial memory in the rat. Front. Neural Circ 6, 8. 10.3389/fncir.2012.00008.

Amelio I, Panatta E, Niklison-Chirou MV, Steinert JR, Agostini M, Morone N, Knight RA, and Melino G (2020). The C terminus of p73 is essential for hippocampal development. Proc. Natl. Acad. Sci. U S A 117, 15694–15701. 10.1073/pnas.2000917117. [PubMed: 32571922]

Anstötz M, Huang H, Marchionni I, Haumann I, Maccaferri G, and Lübke JH (2016). Developmental profile, morphology, and synaptic connectivity of Cajal-Retzius Cells in the postnatal mouse hippocampus. Cereb. Cortex 26, 855–872. 10.1093/cercor/bhv271. [PubMed: 26582498]

Anstötz M, Lee SK, Neblett TI, Rune G, and Maccaferri G (2018a). Experience-dependent regulation of Cajal-Retzius cell networks in the developing and adult mouse hippocampus. Cereb. Cortex 28, 672–687. 10.1093/cercor/bhx153. [PubMed: 28637318]

Anstötz M, Quattrocolo G, and Maccaferri G (2018b). Cajal-Retzius cells and GABAergic interneurons of the developing hippocampus: close electrophysiological encounters of the third kind. Brain Res. 1697, 124–133. 10.1016/j.brainres.2018.07.028. [PubMed: 30071194]

Anstötz M, and Maccaferri G (2020). A toolbox of criteria for distinguishing cajal-retzius cells from other neuronal types in the postnatal mouse Hippocampus. eNeuro 7, 1. 10.1523/ENEURO.0516-19.2019.

Baloyannis SJ (2005). Morphological and morphometric alterations of Cajal-Retzius cells in early cases of Alzheimer's disease: a Golgi and electron microscope study. Int. J. Neurosci 115, 965–980. 10.1080/00207450590901396. [PubMed: 16051543]

Blackstad TW (1975). Electron microscopy of experimental axonal degeneration in photochemically modified Golgi preparations: a procedure for precise mapping of nervous connections. Brain Res. 95, 191–210. 10.1016/0006-8993(75)90101-8. [PubMed: 1098734]

Blümcke I, Beck H, Suter B, Hoffmann D, Födisch HJ, Wolf HK, Elger CE, and Wiestler OD (1999). An increase of hippocampal calretinin-immunoreactive neurons correlates with early febrile seizures in temporal lobe epilepsy. Acta Neuropathol. 97, 31–39. 10.1007/s004010050952. [PubMed: 9930892]

Bourin M, and Hascoët M (2003). The mouse light/dark box test. Eur. J. Pharmacol 463, 55–65. 10.1016/s0014-2999(03)01274-3. [PubMed: 12600702]

Broadbent NJ, Squire LR, and Clark RE (2004). Spatial memory, recognition memory, and the hippocampus. Proc. Natl. Acad. Sci. USA 101, 14515–14520. 10.1073/pnas.0406344101. [PubMed: 15452348]

Causeret F, Moreau MX, Pierani A, and Blanquie O (2021). The multiple facets of Cajal-Retzius neurons. Development 148, dev199409. 10.1242/dev.199409. [PubMed: 34047341]

Caviness VS Jr., and Sidman RL (1973a). Retrohippocampal, hippocampal and related structures of the forebrain in the reeler mutant mouse. J. Comp. Neurol 147, 235–253. 10.1002/cne.901470206. [PubMed: 4682775]

Caviness VS Jr., and Sidman RL (1973b). Time of origin of corresponding cell classes in the cerebral cortex of normal and reeler mutant mice: an auto-radiographic analysis. J. Comp. Neurol 148, 141–151. 10.1002/cne.901480202. [PubMed: 4700506]

Chowdhury TG, Jimenez JC, Bomar JM, Cruz-Martin A, Cantle JP, and Portera-Cailliau C (2010). Fate of cajal-retzius neurons in the postnatal mouse neocortex. Front. Neuroanat 4, 10. 10.3389/neuro.05.010.2010. [PubMed: 20339484]

Daniels RW, Collins CA, Chen K, Gelfand MV, Featherstone DE, and DiAntonio A (2006). A single vesicular glutamate transporter is sufficient to fill a synaptic vesicle. Neuron 49, 11–16. 10.1016/j.neuron.2005.11.032. [PubMed: 16387635]

D'Arcangelo G, Miao GG, Chen SC, Scares HD, Soares HD, Morgan JI, and Curran T (1995). A protein related to extracellular matrix proteins deleted in the mouse mutant reeler. Nature 374, 719–723. 10.1038/374719a0. [PubMed: 7715726]

de Frutos CA, Bouvier G, Arai Y, Thion MS, Lokmane L, Keita M, Garcia-Dominguez M, Charnay P, Hirata T, Riethmacher D, et al. (2016). Reallocation of olfactory cajal-retzius cells shapes neocortex architecture. Neuron 92, 435–448. 10.1016/j.neuron.2016.09.020. [PubMed: 27693257]

del Río JA, Martínez A, Fonseca M, Auladell C, and Soriano E (1995). Glutamate-like immunoreactivity and fate of Cajal-Retzius cells in the murine cortex as identified with calretinin antibody. Cereb. Cortex 5, 13–21. 10.1093/cercor/5.1.13. [PubMed: 7719127]

Del Río JA, Heimrich B, Borrell V, Förster E, Drakew A, Alcántara S, Nakajima K, Miyata T, Ogawa M, Mikoshiba K, et al. (1997). A role for Cajal-Retzius cells and reelin in the development of hippocampal connections. Nature 385, 70–74. 10.1038/385070a0. [PubMed: 8985248]

Derer P, and Derer M (1990). Cajal-Retzius cell ontogenesis and death in mouse brain visualized with horseradish peroxidase and electron microscopy. Neuroscience 36, 839–856. 10.1016/0306-4522(90)90027-2. [PubMed: 2234416]

Desmond NL, Scott CA, Jane JA Jr., and Levy WB (1994). Ultrastructural identification of entorhinal cortical synapses in CA1 stratum lacunosum-moleculare of the rat. Hippocampus 4, 594–600. 10.1002/hipo.450040509. [PubMed: 7534172]

Durand GM, Kovalchuk Y, and Konnerth A (1996). Long-term potentiation and functional synapse induction in developing hippocampus. Nature 381, 71–75. 10.1038/381071a0. [PubMed: 8609991]

Engin E, Smith KS, Gao Y, Nagy D, Foster RA, Tsvetkov E, Keist R, Crestani F, Fritschy JM, Bolshakov VY, et al. (2016). Modulation of anxiety and fear via distinct intrahippocampal circuits. Elife 5, e14120. 10.7554/eLife.14120. [PubMed: 26971710]

Frotscher M (1998). Cajal-Retzius cells, Reelin, and the formation of layers. Curr. Opin. Neurobiol 8, 570–575. 10.1016/s0959-4388(98)80082-2. [PubMed: 9811621]

Gil V, Nocentini S, and del RÃ-o JA (2014). Historical first descriptions of Cajal-Retzius cells: from pioneer studies to current knowledge. Front. Neuroanat 8, 32. 10.3389/fnana.2014.00032. [PubMed: 24904301]

Goffinet AM (1984). Events governing organization of postmigratory neurons: studies on brain development in normal and reeler mice. Brain Res. 7, 261–296. 10.1016/0165-0173(84)90013-4.

Griveau A, Borello U, Causeret F, Tissir F, Boggetto N, Karaz S, and Pierani A (2010). A novel role for Dbx1-derived Cajal-Retzius cells in early regionalization of the cerebral cortical neuroepithelium. PLoS Biol. 8, e1000440. 10.1371/journal.pbio.1000440. [PubMed: 20668538]

Hales JB, Schlesiger MI, Leutgeb JK, Squire LR, Leutgeb S, and Clark RE (2014). Medial entorhinal cortex lesions only partially disrupt hippocampal place cells and hippocampus-dependent place memory. Cell Rep. 9, 893–901. 10.1016/j.celrep.2014.10.009. [PubMed: 25437546]

Hanse E, Seth H, and Riebe I (2013). AMPA-silent synapses in brain development and pathology. Nat. Rev. Neurosci 14, 839–850. 10.1038/nrn3642. [PubMed: 24201185]

Hargreaves EL, Rao G, Lee I, and Knierim JJ (2005). Major dissociation between medial and lateral entorhinal input to dorsal hippocampus. Science 308, 1792–1794. 10.1126/science.1110449. [PubMed: 15961670]

Hestrin S, Nicoll RA, Perkel DJ, and Sah P (1990). Analysis of excitatory synaptic action in pyramidal cells using whole-cell recording from rat hippocampal slices. J. Physiol 422, 203–225. 10.1113/jphysiol.1990.sp017980. [PubMed: 1972190]

Hevner RF, Neogi T, Englund C, Daza RA, and Fink A (2003). Cajal-Retzius cells in the mouse: transcription factors, neurotransmitters, and birthdays suggest a pallial origin. Brain Res. Dev. Brain Res 141, 39–53. 10.1016/s0165-3806(02)00641-7. [PubMed: 12644247]

Hu H, Cavendish JZ, and Agmon A (2013). Not all that glitters is gold: off-target recombination in the somatostatin-IRES-Cre mouse line labels a subset of fast-spiking interneurons. Front. Neural Circ 7, 195. 10.3389/fncir.2013.00195.

Ina A, Sugiyama M, Konno J, Yoshida S, Ohmomo H, Nogami H, Shutoh F, and Hisano S (2007). Cajal-Retzius cells and subplate neurons differentially express vesicular glutamate transporters 1 and 2 during development of mouse cortex. Eur. J. Neurosci 26, 615–623. 10.1111/j.1460-9568.2007.05703.x. [PubMed: 17651422]

Kwon HB, and Sabatini BL (2011). Glutamate induces de novo growth of functional spines in developing cortex. Nature 474, 100–104. 10.1038/nature09986. [PubMed: 21552280]

Shan X, Contreras MP, Mendez M, Born J, Inostroza M, Witter MP, Moser EI, and Moser MB (2010). Development of the spatial representation system in the rat. Science 328, 1576–1580. 10.1002/hipo.23392. [PubMed: 20558721]

Ledonne F, Orduz D, Mercier J, Vigier L, Grove EA, Tissir F, Angulo MC, Pierani A, and Coppola E (2016). Targeted inactivation of bax reveals a subtype-specific mechanism of cajal-retzius neuron death in the postnatal cerebral cortex. Cell Rep. 17, 3133–3141. 10.1016/j.celrep.2016.11.074. [PubMed: 28009284]

Louvi A, Yoshida M, and Grove EA (2007). The derivatives of the Wnt3a lineage in the central nervous system. J. Comp. Neurol 504, 550–569. 10.1002/cne.21461. [PubMed: 17701978]

Livak KJ, and Schmittgen TD (2001). Analysis of relative gene expression data using real-time quantitative PCR and the 2–ΔΔCT method. Methods 25, 402–408. 10.1006/meth.2001.1262. [PubMed: 11846609]

Madisen L, Mao T, Koch H, Zhuo JM, Berenyi A, Fujisawa S, Hsu YWA, Garcia AJ 3 rd, Gu X, Zanella S, et al. (2012). A toolbox of Cre-dependent optogenetic transgenic mice for light-induced activation and silencing. Nat. Neurosci 15, 793–802. 10.1038/nn.3078. [PubMed: 22446880]

Marchionni I, Takács VT, Nunzi MG, Mugnaini E, Miller RJ, and Maccaferri G (2010). Distinctive properties of CXC chemokine receptor 4-expressing Cajal-Retzius cells versus GABAergic interneurons of the postnatal hippocampus. J. Physiol 588, 2859–2878. 10.1113/jphysiol.2010.190868. [PubMed: 20547684]

Mattison HA, Popovkina D, Kao JPY, and Thompson SM (2014). The role of glutamate in the morphological and physiological development of dendritic spines. Eur. J. Neurosci 39, 1761–1770. 10.1111/ejn.12536. [PubMed: 24661419]

Moser EI, Moser MB, and McNaughton BL (2017). Spatial representation in the hippocampal formation: a history. Nat. Neurosci 20, 1448–1464. 10.1038/nn.4653. [PubMed: 29073644]

Müller-Komorowska D, Opitz T, Elzoheiry S, Schweizer M, Ambrad Giovannetti E, and Beck H (2020). Nonspecific expression in limited excitatory cell populations in interneuron-targeting Cre-driver lines can have large functional effects. Front. Neural Circ 14, 16. 10.3389/fncir.2020.00016.

Newell AJ, Lalitsasivimol D, Willing J, Gonzales K, Waters EM, Milner TA, McEwen BS, and Wagner CK (2018). Progesterone receptor expression in cajal-retzius cells of the developing rat dentate gyrus: potential role in hippocampus-dependent memory. J. Comp. Neurol 526, 2285–2300. 10.1002/cne.24485. [PubMed: 30069875]

Newell AJ, Chung SH, and Wagner CK (2021). Inhibition of progesterone receptor activity during development increases reelin-immunoreactivity in Cajal-Retzius cells, alters synaptic innervation in neonatal dentate gyrus, and impairs episodic-like memory in adulthood. Horm. Behav 127, 104887. 10.1016/j.yhbeh.2020.104887. [PubMed: 33166560]

Ogawa M, Miyata T, Nakajimat K, Yagyu K, Seike M, Ikenaka K, Yamamoto H, and Mikoshibat K (1995). The reeler gene-associated antigen on Cajal-Retzius neurons is a crucial molecule for laminar organization of cortical neurons. Neuron 14, 899–912. 10.1016/0896-6273(95)90329-1. [PubMed: 7748558]

Osheroff H, and Hatten ME (2009). Gene expression profiling of preplate neurons destined for the subplate: genes involved in transcription, axon extension, neurotransmitter regulation, steroid hormone signaling, and neuronal survival. Cereb. Cortex 19 (Suppl 1), i126–i134. 10.1093/cercor/bhp034. [PubMed: 19398467]

Quattrocolo G, and Maccaferri G (2013). Novel GABAergic circuits mediating excitation/inhibition of Cajal-Retzius cells in the developing hippocampus. J. Neurosci 33, 5486–5498. 10.1523/JNEUROSCI.5680-12.2013. [PubMed: 23536064]

Quattrocolo G, and Maccaferri G (2014). Optogenetic activation of Cajal-Retzius cells reveals their glutamatergic output and a novel feed-forward circuit in the developing mouse hippocampus. J. Neurosci 34, 13018–13032. 10.1523/JNEUROSCI.1407-14.2014. [PubMed: 25253849]

Rice DS, and Curran T (2001). Role of the reelin signaling pathway in central nervous system development. Annu. Rev. Neurosci 24, 1005–1039. 10.1146/annurev.neuro.24.1.1005. [PubMed: 11520926]

Riva M, Genescu I, Habermacher C, Orduz D, Ledonne F, Rijli FM, López-Bendito G, Coppola E, Garel S, Angulo MC, and Pierani A (2019). Activity-dependent death of transient Cajal-Retzius neurons is required for functional cortical wiring. Elife 8, e50503. 10.7554/eLife.50503. [PubMed: 31891351]

Rodgers RJ, and Dalvi A (1997). Anxiety, defence and the elevated plus maze. Neurosci. Biobehav. Rev 21, 801–810. 10.1016/s0149-7634(96)00058-9. [PubMed: 9415905]

Rose CR, Felix L, Zeug A, Dietrich D, Reiner A, and Henneberger C (2018). Astroglial glutamate signaling and uptake in the Hippocampus. Front. Mol. Neurosci 10, 451. 10.3389/fnmol.2017.00451. [PubMed: 29386994]

Schneider CA, Rasband WS, and Eliceiri KW (2012). NIH Image to ImageJ: 25 years of image analysis. Nat. Methods 9, 671–675. 10.1038/nmeth.2089. [PubMed: 22930834]

Simon P, Dupuis R, and Costentin J (1994). Thigmotaxis as an index of anxiety in mice: influence of dopaminergic transmissions. Behav. Brain Res 61, 59–64. 10.1016/0166-4328(94)90008-6. [PubMed: 7913324]

Soda T, Nakashima R, Watanabe D, Nakajima K, Pastan I, and Nakanishi S (2003). Segregation and coactivation of developing neocortical layer 1 neurons. J. Neurosci 23, 6272–6279.10.1523/JNEUROSCI.23-15-06272.2003. [PubMed: 12867512]

Tissir F, Ravni A, Achouri Y, Riethmacher D, Meyer G, and Goffinet AM (2009). DeltaNp73 regulates neuronal survival *in vivo*. Proc. Natl. Acad. Sci. U S A 106, 16871–16876. 10.1073/pnas.0903191106. [PubMed: 19805388]

Villar-Cerviño V, and Marín O (2012). Cajal-Retzius cells. Curr. Biol 22, R179. 10.1016/j.cub.2012.01.016. [PubMed: 22440796]

von Haebler D, Stabel J, Draguhn A, and Heinemann U (1993). Properties of horizontal cells transiently appearing in the rat dentate gyrus during ontogenesis. Exp. Brain Res 94, 33–42. 10.1007/BF00230468. [PubMed: 7687562]

Wang C, Chen X, Lee H, Deshmukh SS, Yoganarasimha D, Savelli F, and Knierim JJ (2018). Egocentric coding of external items in the lateral entorhinal cortex. Science 362, 945–949. 10.1126/science.aau4940. [PubMed: 30467169]

Wills TJ, Cacucci F, Burgess N, and O'Keefe J (2010). Development of the hippocampal cognitive map in preweanling rats. Science 328, 1573–1576. 10.1126/science.1188224. [PubMed: 20558720]

Yoshida M, Assimacopoulos S, Jones KR, and Grove EA (2006). Massive loss of Cajal-Retzius cells does not disrupt neocortical layer order. Development 133, 537–545. 10.1242/dev.02209. [PubMed: 16410414]

Highlights

- Synaptic output of hippocampal Cajal-Retzius cells (CRs) depends on vGluT2
- Conditional knockout of vGluT2 in CRs is presented
- CR synaptic output regulates innate anxiety and spatial memory
- CR synaptic output shapes feedforward inhibition and synapse maturation

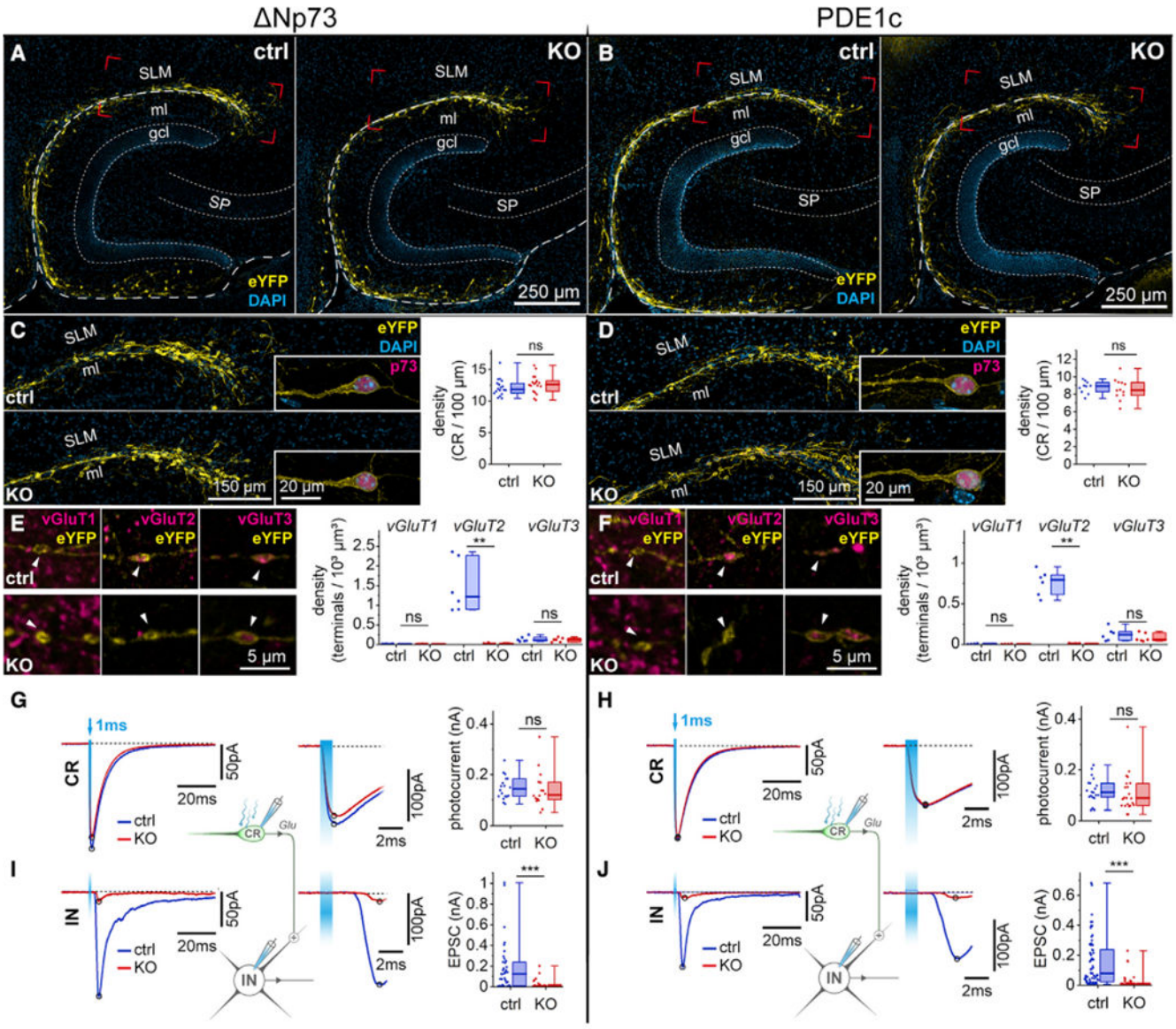

Figure 1. Validation of two distinct conditional vGluT2 KO lines

(A) Left: overview of the hippocampal molecular layers in the ΔNp73-control (ctrl, left) and ΔNp73-KO mouse (KO, right). Expression of ChR2(H134R)-EYFP by CRs in yellow (EYFP). DAPI counterstaining: cyan (DAPI). White dotted lines: borders between layers. SLM, stratum lacunosum moleculare; ml, molecular layer of the dentate gyrus; gcl, granule cell layer; SP, stratum pyramidale.

(B) As in (A) but for PDE1c-ctrl and PDE1c-KO animals.

(C) Left: regions delimited by the red corners in (A). Insets: individual CRs and p73 nuclear immunoreactivity (magenta). DAPI stain in cyan. Right: summary plot of the linear density of p73-labled CRs in the two genotypes (ctr: blue, KO: red, n = 18 sections and 3 mice per genotype).

(D) As in (C) but for PDE1c-ctrl and PDE1c-KO mice (ctrl, n = 10 sections; KO, n = 12 sections, 3 mice per genotype).

(E) Left: immunoreactivity of EYFP+ CR terminals (yellow) for vGluT1, vGluT2, and vGluT3 (magenta) in ΔNp73-ctrl (top row) and ΔNp73-KO animals (bottom row). Right: quantification of bouton density according to their specific vGluT labeling (vGluT1, vGluT2, and vGluT3) and genotype (ctrl; KO, n = 6 stacks, 3 mice per genotype).
(F) As in (E) but for PDE1c-ctrl and PDE1c-KO mice (n = 6 stacks, 3 mice per genotype). P30 animals.
(G) Flash-evoked photocurrents in CRs. Left: averaged traces of photocurrents in ΔNp73-ctrl (ctrl, blue, n = 18 cells, 3 mice) and ΔNp73-KO animals (KO, red, n = 16 cells, 2 mice) are superimposed. Vholding = −60 mV. Circle: current peak; light blue arrow: time of the flash (1 ms duration). Middle: same traces at an expanded timescale. Notice the nearly instantaneous photocurrent during the flash (light blue shaded area). Right: summary plot of all experiments.
(H) As in (G) but for PDE1c-ctrl and PDE1c-KO animals (ctrl, n = 22 cells, 5 mice, and KO, n = 20 cells, 8 mice).
(I) Postsynaptic responses generated by CRs on interneurons (INs). Left, averaged EPSCs in INs of the molecular layers, following the optogenetic stimulation of CRs (light blue area). Vholding = −60 mV. Middle: same traces at a different timescale. In contrast to the photocurrents in (G), the EPSC follows the flash. Right: summary graph showing impaired transmission in KO (n = 27 cells, 4 mice) versus ctrl animals (n = 38 cells, 7 mice). The schematic shows the direct recording of flash-evoked (blue lightning) photocurrents from a CR and of EPSCs from an IN. The excitatory and glutamatergic nature of the connection is indicated by the (+) symbol and (Glu), respectively.
(J) As in (I) but for PDE1c-ctrl (n = 66 cells, 10 mice) and PDE1c-KO mice (n = 48 cells, 9 mice). Boxplots: median (middle dash), lower and upper quartiles (box borders), and minimum and maximum (whiskers).
ns, $p > 0.05$; *$p < 0.05$; and **$p < 0.01$.

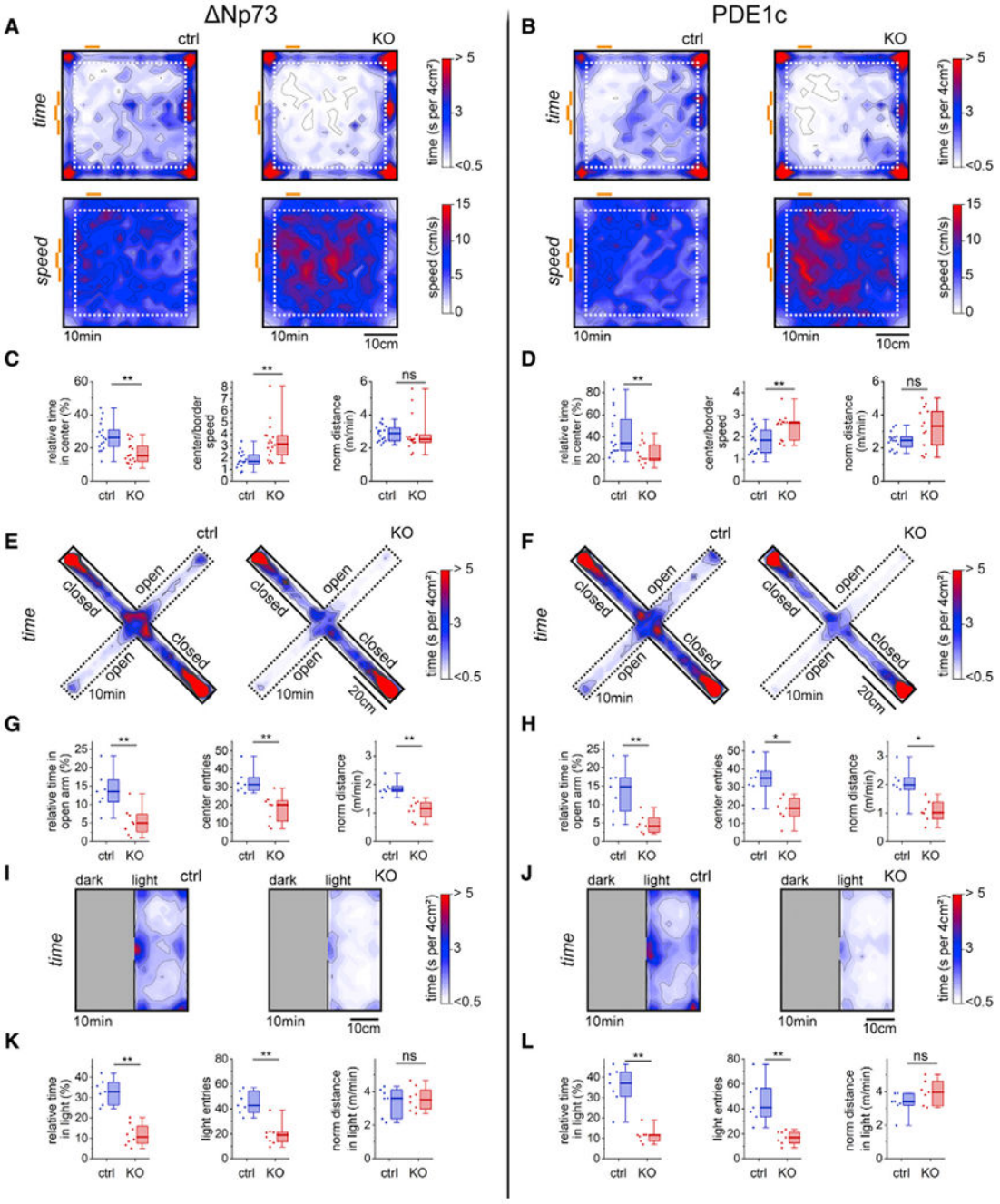

Figure 2. Increased innate anxiety in ΔNp73- and PDE1c-KO mice

(A) Upper row: averaged heatmaps of the time spent at specific locations in open-field tests for ΔNp73-ctrl (ctrl, left, n = 17) and ΔNp73-KO (KO, right, n = 18) animals. Notice the aversion of KO mice for the central area compared with the border closer to the walls (delimited by the white dotted line). Lower row: averaged heatmaps of the speed of the animals. Thick orange stripes: environmental cues.

(B) As in (A) but for PDE1c-ctrl (n = 16) and PDE1c-KO (n = 13) mice.

(C) Summary plots of the relative time spent in the center (left), ratio of center/border speed (middle), and normalized distance traveled (right) by ΔNp73-ctrl and ΔNp73-KO mice. Notice the enhanced central avoidance in KO mice, despite the normalized distance traveled similar to ctrl animals.
(D) Same organization as in (C) but for PDE1c-ctrl (n = 16) and PDE1c-KO mice (n = 13).
(E) Elevated plus maze test: averaged heatmaps for ΔNp73-ctrl (ctrl, left, n = 7) and ΔNp73-KO (KO, right, n = 8) animals. In contrast to the open arms (open) of the plus-shaped platform, closed arms are protected by walls (closed). KO mice show increased tendency to avoid the open space.
(F) As in (E) but for PDE1c-ctrl (n = 7) and PDE1c-KO (n = 7) animals.
(G) Summary boxplots of the relative time spent in the open arm (left), number of center entries (middle), and normalized distance traveled (right). Notice the aversion for the open arm and the decreased exploratory activity.
(H) Same organization as in (G) but for PDE1c-ctrl and PDE1c-KO animals.
(I) Averaged heatmaps for the light/dark transitions task for ΔNp73-ctrl (ctrl, left, n = 7) and ΔNp73-KO (KO, right, n = 8) mice. The left half of the arena (grey) is covered and kept in the dark, whereas the right half is illuminated. KO mice have increased preference for the darker compartment.
(J) As in (I) but for PDE1c-ctrl (n = 7) and PDE1c-KO (n = 7) animals.
(K) Summary quantification of the relative time spent in the light area (left), number of entries in the light compartment (middle), and normalized traveled distance (evaluated in the illuminated area, right).
(L) As in (K) but for PDE1c-ctrl and PDE1c-KO mice. Boxplots: median (middle dash), lower and upper quartiles (box borders), and minimum and maximum (whiskers).
ns, $p > 0.05$; *$p < 0.05$; and **$p < 0.01$.

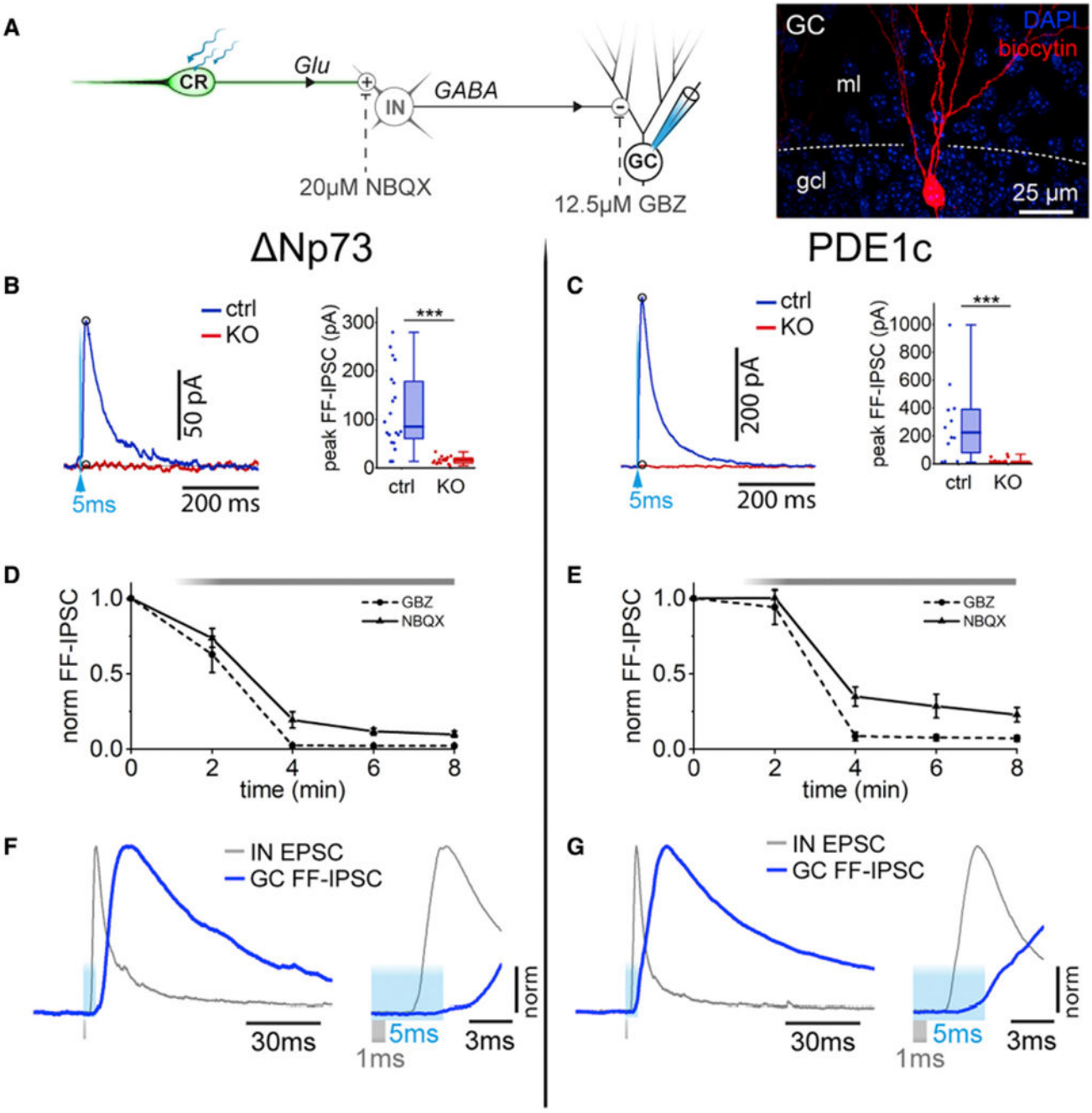

Figure 3. Loss of CR-dependent feedforward inhibition in the dentate gyrus of ΔNp73- and PDE1c-KO mice

(A) Left: circuit involved in flash-evoked (light blue lightning) feedforward IPSCs recorded from granule cells. CR, Cajal-Retzius cell; IN, interneuron; GC, granule cell. (+) and (Glu), excitatory and glutamatergic connection; (−) and GABA:, inhibitory and GABAergic synapse. Dotted lines: blocking action of the drugs. Right: GC filled with biocytin (red). Dotted line: fissure. ml, molecular layer; gcl, granule cell layer. DAPI counterstain: blue.

(B) Left, averaged flash-evoked (light blue arrow) feedforward IPSCs in GCs of ΔNp73-ctrl (ctrl, blue, n = 20 cells, 5 mice) and ΔNp73-KO mice (KO, red, n = 16 cells, 3 mice). Right: summary plot comparing responses in KO versus control animals.
(C) As in (B) but for PDE1c-ctrl (n = 27 cells, 2 mice) and PDE1c-KO mice (n = 12 cells, 3 mice).
(D) Time course of the block of the normalized feedforward IPSC (norm FF-IPSC) in control mice by either gabazine (GBZ, 12.5 μM, dotted line, n = 7 cells, 2 mice) or NBQX (NBQX, 20 μM, solid line, n = 9 cells, 3 mice). Gray bar: drug application. The sensitivity of the flash-evoked response to GBZ and NBQX demonstrates its feedforward nature.
(E) As in (D) but for PDE1c-ctrl and PDE1c-KO animals (GBZ, n = 8 cells, 2 mice, and NBQX, n = 14 cells, 6 mice).
(F) Left: super imposition of the normalized averaged monosynaptic EPSC recorded from INs (gray, data from Figure 1) with the normalized averaged FF-IPSC (blue). Both waveforms (from ΔNp73-ctrl mice) are positive going to facilitate the comparison. Right: different timescale. Despite the shorter-duration flash (1 ms, gray downward shaded area) used for the monosynaptic response (compared with 5 ms used for the FF-IPSC, blue upward shaded area), the FF-IPSC has a longer latency and slower risetime, indicative of its polysynaptic and compound nature.
(G) As in (F) but for PDE1c-ctrl mice. Boxplots: median (middle dash), lower and upper quartiles (box borders), and minimum and maximum (whiskers).
***$p < 0.001$.

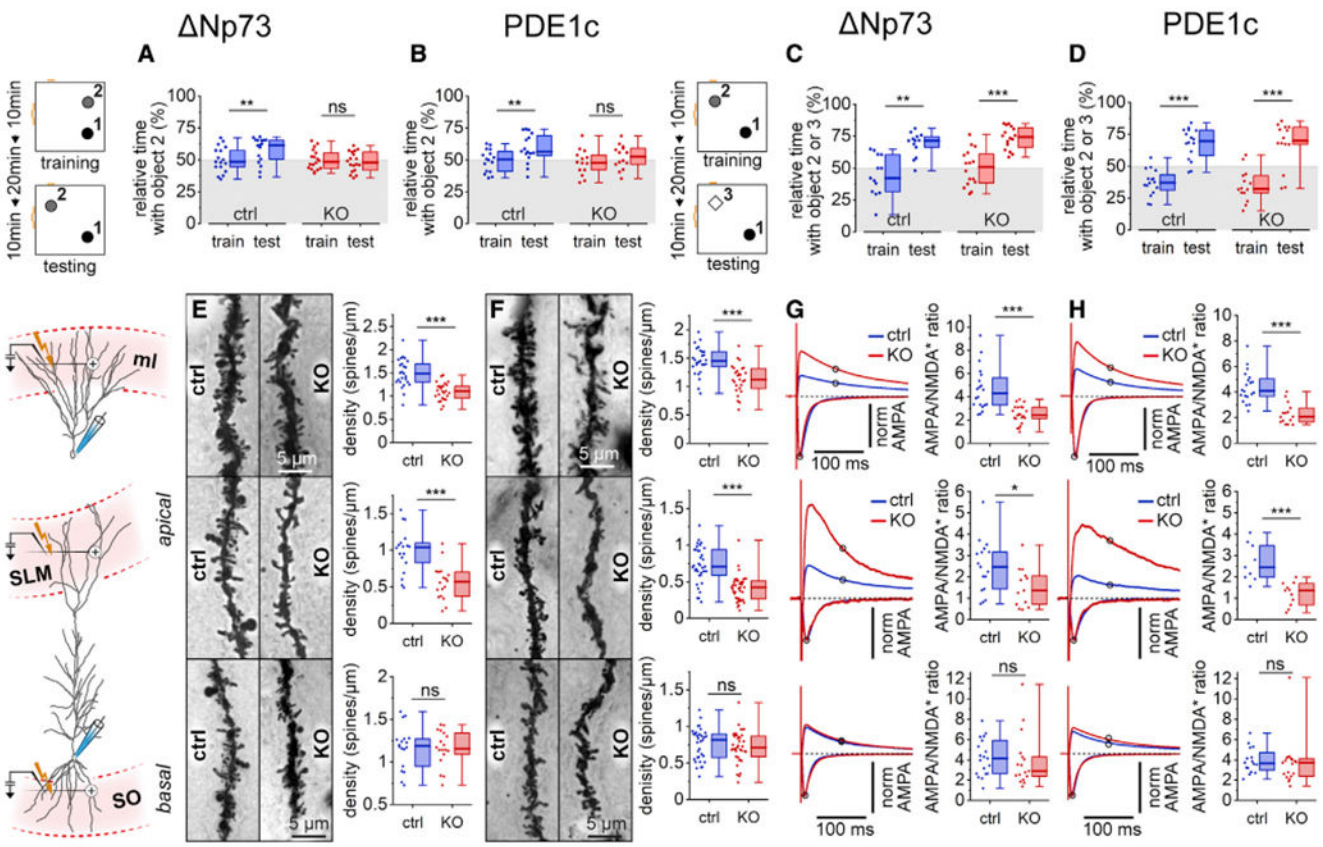

Figure 4. The selective impairment in spatial memory of ΔNp73- and PDE1c-KO mice is associated with layer-specific loss of dendritic spines and reduced AMPA/NMDA ratio of electrically evoked EPSCs

(A) Left: object-location test. Arena (box) with environmental cues (thick orange stripes) and two objects (object1, black filled circle, and object2, grey filled circle). Object2 is moved to a different spot for the testing phases. Right: summary plots of the relative time spent by the mice in proximity of object2 (relative to the total time spent close to object1 and object2) according to the phase of the experiment (training: train; testing: test) and genotype (ΔNp73-ctrl: ctrl, n = 17; DNp73-KO: KO, n = 18). Relative time spent with the moved object increases in ctrl, but not in KO, mice.

(B) As in (A) but for PDE1c-ctrl (n = 16) and PDE1c-KO (n = 14) animals.

(C) Left: novel-object-recognition test during the training and testing phases. Object2 (grey filled circle) is replaced by object3 (empty diamond) in the testing phase. Right: summary graphs of the relative time spent in proximity to object2 during training (and to object3 during testing) relative to the total time spent with object1 and object2 during training (and object1 and object3 during testing). Data sorted according to phase and genotype (ΔNp73-ctrl: ctrl; ΔNp73-KO: KO). Both ctrl (n = 13) and KO (n = 16) mice increase their preference for the unfamiliar object in the testing phase.

(D) As in (E) but for PDE1c-ctrl (n = 16) and PDE1c-KO (n = 14) mice.

(E) Left: reconstructions of a biocytin-filled GC (top) and of a CA1 pyramidal neuron (PC; bottom) from a ΔNp73-ctrl mouse. The regions used for spine-density quantification are indicated by the light red area delimited by the red dotted lines. Electrical stimulation is

indicated by the thin black electrode and yellow lightening. Responses are purely excitatory (+) because of added GBZ (12.5 μM). ml, distal half of the molecular layer of the dentate gyrus; SLM, stratum lacunosum moleculare; SO, stratum oriens. Middle: dendritic spines (Golgi stain) from ΔNp73-ctrl (ctrl) and ΔNp73-KO (KO) mice in GCs (top) and in apical (middle) or basal (bottom) dendrites of PCs. Right: summary plots. Notice the decreased spine density in KO mice, limited to the dendrites in the molecular layers (ctrl and KO GCs, n = 25 and n = 26 dendrites, respectively; ctrl and KO PCs, 18 dendrites each in SLM) as opposed to those in stratum oriens (ctrl and KO PCs, n = 18 dendrites each in SO). 3 mice per genotype, P30.

(F) As in (E) but for PDE1c-ctrl and PDE1c-KO mice (ctrl and KO GCs, n = 27 dendrites each, ctrl and KO PC, n = 35 and n = 39 dendrites in SLM, and ctrl and KO PCs, n = 33 and n = 37 dendrites in SO). 3 mice per genotype, P30.

(G) Left: averaged evoked EPSCs recorded in GCs (top, ml stimulation) and PCs (middle, SLM stimulation; bottom, SO stimulation) from ΔNp73-ctrl (ctrl, blue) and ΔNp73-KO (KO, red) mice at Vholding = −60 mV (inward currents) and +40 mV (outward currents). Traces normalized to the peak of the inward currents (norm AMPA). Circles: times of measurements (peak of inward currents [AMPA] and after 75 ms for outward currents [NMDA*]). Right: summary plots of AMPA/NMDA* ratios in ctrl versus KO mice according to cell type and stimulus location. Stimulation of ml (ctrl, n = 20 and KO, n = 22 GCs, 5 and 4 mice, respectively) and SLM (ctrl, n = 19 and KO, n = 17 PCs, 4 mice per genotype) produces different AMPA/NMDA* ratios in KO versus control animals, in contrast to responses triggered by SO stimulation (ctrl, n = 19, and KO, n = 17 PCs, 4 mice per genotype).

(H) As in (G) but for PDE1c-ctrl and -KO animals (ctrl, n = 20 and KO, n = 15 GCs, 4 and 2 mice, respectively; ctrl n = 9 and ctrl KO n = 11 PCs for SLM stimulation, 4 and 3 mice, respectively; ctrl, n = 16 and KO n = 19 PCs for SO stimulation, 4 and 3 mice, respectively). Boxplots: median (middle dash), lower and upper quartiles (box borders), and minimum and maximum (whiskers).

ns, $p > 0.05$; *$p < 0.05$; **$p < 0.01$; and ***$p < 0.001$.

KEY RESOURCES TABLE

REAGENT or RESOURCE	SOURCE	IDENTIFIER
Antibodies		
Rabbit anti-p73	Abcam	Cat# ab40658; RRID: AB_776999
Mouse anti-reelin	Millipore	Cat# MAB5364: RRID: AB_11212203
Rabbit anti-GAD67	Abcam	Cat# ab97739; RRID:AB_10681171
Rabbit anti-vGluT1	Synaptic Systems	Cat# 135308; RRID:AB_2864787
Rabbit anti-vGluT2	Synaptic Systems	Cat# 135408, RRID:AB_2864778
Rabbit anti-vGluT3	Synaptic Systems	Cat# 135208; RRID:AB_2884933
Alexa Fluor 568 goat anti-rabbit IgG	Thermo Fisher Scientific	Cat# A-11036; RRID:AB_10563566
Alexa Fluor 568 goat anti-mouse IgG	Thermo Fisher Scientific	Cat# A-11004; RRID:AB_2534072
Alexa Fluor 647 goat anti-rabbit IgG	Thermo Fisher Scientific	Cat# A32733; RRID:AB_2633282
Alexa Fluor 647 goat anti-mouse IgG	Thermo Fisher Scientific	Cat# A28181; RRID:AB_2536165
Mouse anti-α-Tubulin	Sigma-Aldrich	Cat# T6199; RRID: AB_477583
Rabbit anti GAD 65/67	Sigma-Aldrich	Cat# ABN904; RRID: AB_2893025
Chemicals, peptides, and recombinant proteins		
Gabazine	Abcam	Cat# ab120042; CAS: 104104-50-9
NBQX	Abcam	Cat# ab120045; CAS: 118876-58-7
DAPI	Thermo Fisher Scientific	Cat#62248
QIAGEN® RNase Inhibitor	QIAGEN	Cat# 129916
DNase I	QIAGEN	Cat# 79254
RT^2 First Strand Kit	QIAGEN	Cat# 330401
streptavidin-Alexa™ 568	Invitrogen	Cat# S11226
RIPA Lysis Buffer System	Santa Cruz Biotechnology	Cat# sc-24948
NuPAGE™ LDS Sample Buffer	Invitrogen	Cat# NP0007
NuPAGE™ Sample Reducing Agent	Invitrogen	Cat# NP0009
NuPAGE™ 3 to 8%, Tris-Acetate, 1.0 mm, Mini Protein Gel, 12-well	Invitrogen	Cat# EA03752
Immun-Blot® Low Fluorescence PVDF/Filter Paper Sets	BIO-RAD	Cat# 1620260
NuPAGE™ Transfer Buffer	Invitrogen	Cat# NP0006
NuPAGE™ Antioxidant	Invitrogen	Cat# NP0005
Ponceau S staining solution	Sigma	Cat# P7170
WesternDot™ 625 Goat Anti-Mouse Western Blot Kit	Invitrogen	Cat# W10132
WesternDot™ 625 Goat Anti-Rabbit Western Blot Kit	Invitrogen	Cat# W10142
Critical commercial assays		
FD Rapid Golgi Stain Kit	FD NeuroTechnologies, Inc.	Cat# PK401
VECTASTAIN Elite ABC HRP Kit	Vector Laboratories	Cat# PK-6100
Mowiol® 4-88	Sigma Aldrich	Cat# 81381
QIAshredder	QIAGEN	Cat# 79654
RNeasy Mini Kit	QIAGEN	Cat# 74104

REAGENT or RESOURCE	SOURCE	IDENTIFIER
TaqMan® Assay Reln	Thermo Fisher Scientific	Cat# Mm00465200_m1
TaqMan® Assay Hprt	Thermo Fisher Scientific	Cat# Mm03024075_m1
Pierce™ BCA Protein Assay Kit	Thermo Fisher Scientific	Cat# 23227
Experimental models: Organisms/strains		
ΔNp73-Cre-IRES-GFP	Dr Fadel Tissir, UC Louvain, Belgium	Tissir et al. (2009)
B6.FVB(Cg)-Tg(Pde1c-cre)IT146Gsat/Mmucd	MMRRC	stock number: 036699-UCD; RRID:MMRRC_036699-UCD
B6; 129S-Gt(ROSA)26Sortm32(CAG-COP4*H134R/eYFP)Hze/J	The Jackson Laboratory	stock number 012569, RRID:IMSR_JAX:012569
STOCK Slc17a6tm1Lowl/J	The Jackson Laboratory	stock number 012898, RRID:IMSR_JAX:012898
Software and algorithms		
pClamp10	Axon Instruments	https://www.moleculardevices.com
ImageJ	Schneider et al. (2012)	https://imagej.nih.gov/ij/
Origin 2020	OriginLab	https://originlab.com
Neurolucida 11	MBF Bioscience	https://www.mbfbioscience.com